



# LFD (v1.0): Latent-Compression-Free Generative Diffusion with Geological Priors and Geophysical Regularization for Implicit Structural Modeling

Zhixiang Guo<sup>1,2,3,4</sup>, Xinming Wu<sup>1,2,3</sup>, Yimin Dou<sup>1,2,3</sup>, Hui Gao<sup>1,2,3</sup>, and Guillaume Caumon<sup>4,5</sup>

<sup>1</sup>Laboratory of Seismology and Physics of the Earth's Interior, School of Earth and Space Sciences, University of Science and Technology of China, Hefei, 230026, China

<sup>2</sup>State Key Laboratory of Precision Geodesy, University of Science and Technology of China, Hefei, 230026, China

<sup>3</sup>Mengcheng National Geophysical Observatory, University of Science and Technology of China, Hefei, 230026, China

<sup>4</sup>Université de Lorraine, CNRS, GeoRessources, F-54000 Nancy, France

<sup>5</sup>Institut Universitaire de France (IUF), Paris, France

**Correspondence:** Xinming Wu (xinmwu@ustc.edu.cn)

**Abstract.** Diffusion models provide a promising way to model the distribution of implicit structural models, potentially improving generalization across surveys. However, existing diffusion Transformer pipelines scale poorly to high-dimensional geophysical data because noise- or velocity-prediction objectives are often unstable at large patch sizes, forcing the use of small patches that lead to long token sequences and high computational cost. To reduce computation, most approaches rely on Variational autoencoders (VAEs) and latent diffusion, but robust pretrained VAEs are scarce in geophysics, and enforcing geological priors in latent space is difficult. To address these scalability bottlenecks and the difficulty of enforcing geological priors in latent space, we propose *Latent-Compression-Free Generative Diffusion (LFD) with Geological Priors and Geophysical Regularization* for implicit structural modeling. Built on flow matching, LFD generates implicit structural models directly in the data space, enabling efficient large-patch Vision Transformer (ViT) inference and allowing fault/horizon constraints and geophysical regularization to be applied explicitly during generation. To strengthen structural conditioning, we design a structure-enhanced Transformer that injects horizon and fault embeddings at multiple layers. We further introduce two prior-guided losses: a horizon loss to match the generated models to the input horizons, and a fault-aware bending-energy term that regularizes smoothness while ignoring stencils across faults. By enforcing these priors directly in the data space, the model is effectively constrained to generate geologically reasonable structures. Experiments on both synthetic data and real surveys validate the effectiveness of LFD for prior-guided implicit structural modeling. Benefiting from large-patch inference, LFD generates a  $512 \times 512$  model in 1.56 s on an NVIDIA H20 GPU. With relative positional encoding, LFD can be extended to higher resolutions via simple adaptation without retraining. Overall, LFD offers new insights into deploying diffusion models for high-dimensional geophysical data, enabling efficient generation with interpretable, prior-guided constraints.



## 1 Introduction

20 Implicit structural modeling aims to recover a continuous subsurface representation from sparse and heterogeneous geological observations. A common formulation estimates an implicit scalar field, often referred to as the relative geological time (RGT), whose iso-surfaces represent stratigraphic interfaces (Mallet, 1989; Houlding, 1994; Lajaunie et al., 1997). Compared with explicit surface-based representations (Caumon et al., 2009), implicit modeling provides a true volumetric description that enables consistent extraction of multiple geological surfaces and unified enforcement of heterogeneous constraints (Maxelon et al., 2009; Caumon et al., 2013; Pizzella et al., 2022; Arienti et al., 2025). As a result, implicit structural models have increasingly been adopted in a wide range of applications, including geological surveying and mapping (MacCormack et al., 2019; Guo et al., 2018), seismic interpretation (Wu and Hale, 2015; Bi et al., 2021; Wu et al., 2023), joint geophysical inversion and imaging (Zheglava et al., 2018; Giraud et al., 2020, 2024), mineral resource and reserve estimation (Vollgger et al., 2015; Zhong et al., 2019), and stratigraphic-domain transformations for subsequent property modeling (Cowan et al., 2002; Mallet, 2004; Wellmann and Caumon, 2018; De la Varga et al., 2019). Moreover, the automated and efficient nature of implicit modeling facilitates iterative updates and provides a principled basis for incorporating geological knowledge and quantifying structural uncertainty (Wellmann and Caumon, 2018; Yang et al., 2019).

Classical approaches formulate implicit structural modeling as a constrained interpolation or PDE-based problem, incorporating horizons, faults, and orientation information through variational formulations, discretized operators, or least-squares criteria on constraints (Calcagno et al., 2008; Caumon et al., 2013; Grose et al., 2021). To estimate the scalar field from sparse spatial constraints, two major numerical routes are commonly adopted (Renaudeau et al., 2019). The first route uses meshfree global interpolation, including radial basis function interpolation (Cowan et al., 2002; Guo et al., 2018; Zhong et al., 2019) and dual kriging with polynomial drift (Chilès et al., 2004; Calcagno et al., 2008; De la Varga et al., 2019; Pizzella et al., 2022), for which the computational cost is primarily driven by the number of constraint points. The second route relies on grid-based discretization, where the scalar field is computed by discrete smooth interpolation on discontinuity-conforming tetrahedral meshes (Frank, 2007; Caumon et al., 2013; Mallet, 2014; Irakarama et al., 2022; Belhachmi et al., 2025), and the cost is dominated by the mesh resolution. Complementary PDE-based formulations solve for the implicit field by propagating interface and orientation constraints via Hamilton-Jacobi equations (Osher, 1993; Hjelle and Petersen, 2011; Gillberg et al., 2014). Across these formulations, explicit treatment of discontinuities induced by faults and unconformities is a key source of algorithmic and computational complexity. Although these approaches can produce geologically meaningful fields, they can become expensive at high resolution and often require re-solving the system when constraints are updated.

More recently, deep learning has accelerated implicit structural modeling by learning data-driven priors and accelerating inference from sparse geological constraints. Existing approaches can be broadly categorized into two paradigms. The first paradigm is coordinate-based implicit neural representation (Hillier et al., 2021; Li et al., 2025; Fan et al., 2025), where a network takes spatial coordinates as input and outputs the scalar value of the implicit field (Kamath et al., 2025). This is typically realized with fully connected networks. This formulation is highly flexible and can naturally support divide-and-conquer strategies, such as solving separate sub-fields over different stratigraphic or temporal intervals and then assembling



them into a globally consistent model (Hillier et al., 2023). The second paradigm is field-based prediction (Wang et al., 2023; Lin et al., 2025), where the input is a structured spatial grid and the network directly maps volumetric observations and  
55 constraint rasters to an implicit field, using convolutional networks (Liu and Durlofsky, 2021; Bi et al., 2022; Zhang et al., 2024) or Transformer architectures to capture both local structure and long-range dependencies (Ren et al., 2025). In both paradigms, geological observations and prior rules can be incorporated through differentiable loss terms that constrain the predicted field to honor horizons, faults, and other structural constraints (Wu et al., 2023; Gao and Wellmann, 2025). Despite this progress, generalization across surveys with different structural styles or acquisition characteristics remains challenging,  
60 and new areas may still require re-training or fine-tuning (Sheng et al., 2025; Guo et al., 2025).

Generative diffusion models learn data-driven priors by modeling the data distribution rather than memorizing samples (Sohl-Dickstein et al., 2015; Shah et al., 2025; Bonnaire et al., 2025). This distributional learning can improve generalization, which is appealing for implicit structural modeling. Methodologically, diffusion models follow two main routes. Discrete-time Denoising Diffusion Probabilistic Models (DDPMs) define a forward process that gradually corrupts data through many small  
65 Gaussian noise increments until it becomes nearly Gaussian, and the reverse model must therefore undo this corruption progressively—removing only a small amount of noise per step to stay close to the target distribution. Consequently, DDPMs generate samples via a multi-step reverse process (Ho et al., 2020; Nichol and Dhariwal, 2021; Choi et al., 2021) and, while conceptually simple, typically require hundreds of sequential denoising steps (i.e., many neural network inferences), making sampling computationally expensive. Continuous-time approaches such as flow matching learn a time-dependent velocity field  
70 and sample by integrating an ordinary differential equation (ODE) (Liu et al., 2022; Lipman et al., 2022), often achieving comparable quality with fewer function evaluations and thus better suiting iterative modeling workflows (Dao et al., 2023; Gat et al., 2024). However, deploying flow matching on high-dimensional geophysical data faces key challenges. Diffusion transformers typically rely on VAE-based latent diffusion for efficiency (Rombach et al., 2022; Peebles and Xie, 2023; Lee et al., 2025), yet robust pretrained VAEs are scarce in geophysics. Moreover, geological priors and spatial data are harder to impose  
75 and interpret in latent space than in data space (Garayt et al., 2025). Finally, even with a VAE, noise or velocity prediction in the diffusion models makes structural conditioning indirect because most geological constraints are naturally defined on the implicit scalar field (Song et al., 2023). Recent studies suggest that directly predicting the clean sample (denoted as  $\mathbf{x}$ ), instead of regressing noise ( $\epsilon$ ) or velocity ( $\mathbf{v}$ ), can improve optimization and enable large-patch ViT inference (Li and He, 2025). This reduces attention cost and can avoid VAE-based compression, while allowing priors to be imposed directly in data space.

80 Motivated by these observations, we propose *Latent-Compression-Free Generative Diffusion (LFD) with Geological Priors and Geophysical Regularization* for implicit structural modeling. Our method is built on three key ideas. First, we adopt an  $\mathbf{x}$ -prediction formulation that directly predicts the implicit structural models in data space, which makes constraint handling more direct and supports large-patch transformer inference without requiring VAE-based latent compression (Sec 2.1). Second, we introduce a structure-enhanced network architecture that incorporates interpreted horizons and faults at multiple network  
85 layers (Sec 2.2), enabling these structural constraints to effectively guide the generation of the implicit structural models. Third, we design prior-guided losses derived from geological and geophysical principles to promote structural consistency in the generated models (Sec 2.3). The trained model can be extended to higher resolutions (e.g., 1024 and 2048) through simple

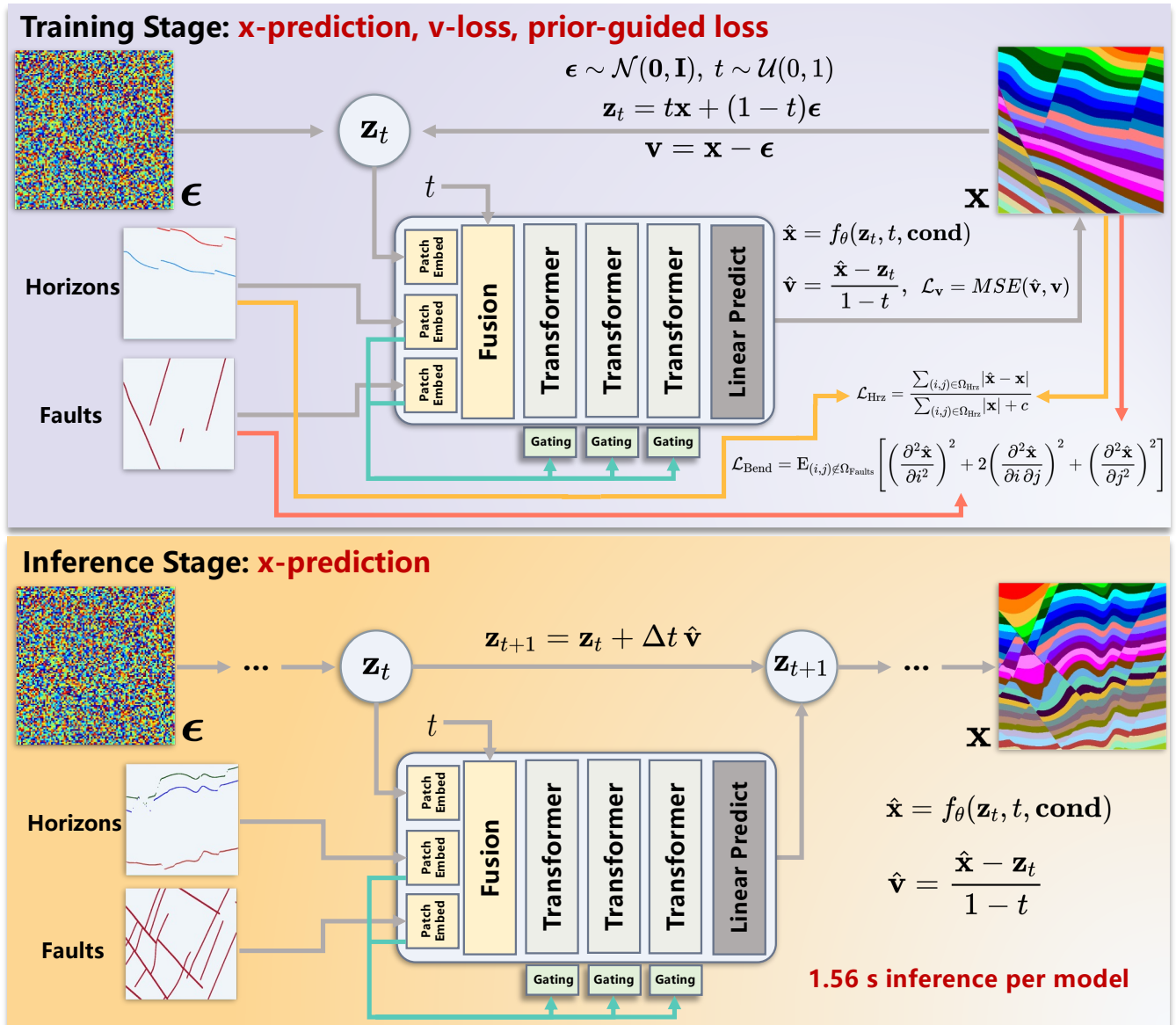


**Figure 1.** Overview of LFD for implicit structural modeling. Top: Training stage. We sample Gaussian noise  $\epsilon$  and time  $t$ , construct  $\mathbf{z}_t = t\mathbf{x} + (1-t)\epsilon$ , and use a structure-enhanced Transformer conditioned on horizons and faults to predict the clean implicit scalar field  $\hat{\mathbf{x}}$ . Bottom: Inference stage. Starting from  $\mathbf{z}_0 = \epsilon$ , we iteratively integrate the probability-flow ODE using  $\hat{\mathbf{x}}$  to obtain  $\hat{\mathbf{v}}$  and generate the final implicit structural model.

adaptations, even when training is performed at 512 resolution. Extensive experiments on synthetic data and real surveys with complex faulting demonstrate that our approach produces more geologically consistent implicit structural models, offering new insights into applying diffusion-based generative modeling to high-dimensional geophysical data (Sec 3).



## 2 Method

This section first reviews the fundamentals of flow-based diffusion models and introduces the  $\mathbf{x}$ -prediction (denoised-sample prediction) formulation adopted in this work. We then present the denoising Transformer architecture, in which interpreted horizons and faults are injected at multiple network layers to ensure that the generated implicit field remains consistent with the input structural constraints. Finally, to better capture the role of structural conditions in generation and to promote geological consistency, we design two prior-guided losses that explicitly enforce structure-consistent learning.

### 2.1 $\mathbf{x}$ -Prediction Diffusion

We briefly review flow matching (Lipman et al., 2022), a generative diffusion framework that learns a continuous transport from a Gaussian base distribution  $\epsilon \sim \mathcal{N}(\mathbf{0}, \mathbf{I})$  to the data distribution  $\mathbf{x} \sim p_{\text{data}}(\mathbf{x})$ . We construct the noisy sample  $\mathbf{z}_t$  at a randomly sampled time  $t \sim \mathcal{U}(0, 1)$  using linear interpolation between the data  $\mathbf{x}$  and Gaussian noise  $\epsilon$ :

$$\mathbf{z}_t = t\mathbf{x} + (1 - t)\epsilon, \quad (1)$$

where  $\mathbf{z}_0 = \epsilon$  and  $\mathbf{z}_1 = \mathbf{x}$ . With the linear interpolation path, the target velocity along this path is constant:

$$\mathbf{v} = \frac{\partial \mathbf{z}_t}{\partial t} = \mathbf{x} - \epsilon, \quad (2)$$

Flow-based methods train a neural network  $f_\theta$  to estimate the velocity field, denoted by  $\hat{\mathbf{v}}$ , where the network takes the time  $t$  and the corresponding noisy sample  $\mathbf{z}_t$  as inputs:

$$\hat{\mathbf{v}} = f_\theta(\mathbf{z}_t, t), \quad (3)$$

The model is optimized by matching  $\hat{\mathbf{v}}$  to  $\mathbf{v}$ :

$$\mathcal{L}_v = \mathbb{E}_{\mathbf{x}, \epsilon, t} \left[ \frac{1}{N} \|\hat{\mathbf{v}} - \mathbf{v}\|_2^2 \right], \quad (4)$$

$\mathcal{L}_v$  minimizes the discrepancy between the target velocity field  $\mathbf{v}$  and its prediction  $\hat{\mathbf{v}}$  via an element-wise mean-squared error over the  $N$  pixels of the field, and the expectation is taken over training samples  $\mathbf{x}$ , Gaussian noise  $\epsilon$ , and randomly sampled times  $t$ . We refer to it as the  $v$ -loss.

At inference, we start from a Gaussian sample  $\mathbf{z}_0 \sim \mathcal{N}(\mathbf{0}, \mathbf{I})$  at  $t = 0$ . We then generate a sample by integrating the learned probability-flow ODE from  $t = 0$  to  $t = 1$ . In practice, we discretize the time interval  $[0, 1]$  into  $K$  uniform steps,  $\{t_k\}_{k=0}^K$ , with  $t_k = k/K$  (thus  $\Delta t = t_{k+1} - t_k = 1/K$ ), and evaluate the network to obtain the velocity field.

$$\hat{\mathbf{v}}_k = f_\theta(\mathbf{z}_{t_k}, t_k), \quad (5)$$

An explicit solver updates the state as

$$\mathbf{z}_{t_{k+1}} = \mathbf{z}_{t_k} + \Delta t \hat{\mathbf{v}}_k, \quad \Delta t = t_{k+1} - t_k, \quad (6)$$



and the final generated sample is obtained at  $t = 1$  as  $\hat{\mathbf{x}} \equiv \mathbf{z}_{t_K}$ . In practice, flow-based sampling typically requires only tens of ODE steps to reach good sample quality (e.g.  $K = 50$ ), which is substantially fewer than the hundreds to thousands of steps often used in DDPM sampling (Zhou et al., 2024).

Learning an accurate velocity field in high-dimensional spaces is challenging for denoisers such as Diffusion Transformers (DiTs) (Peebles and Xie, 2023), often leading to unstable training and reduced sampling efficiency at higher resolutions. As a result,  $v$ -prediction models typically use very small square patches (e.g.,  $2 \times 2$ ,  $4 \times 4$ , or  $8 \times 8$ ), which greatly increases token length and attention cost for large geophysical data (Ma et al., 2024). Most diffusion transformers therefore resort to VAE-based latent diffusion to reduce computation, but this is less appealing for geophysical data because it may compromise fine structural details and makes it harder to explicitly impose geological priors in the latent space.

In contrast, clean samples usually lie on a lower-dimensional manifold (Chapelle et al., 2009), making it easier and more stable to predict the clean signal directly than to regress the velocity field. Recent studies (Li and He, 2025) have demonstrated that directly predicting the clean data  $\mathbf{x}$  combined with the  $v$ -loss leads to more stable optimization and better sample quality. In this setting, the network no longer predicts the velocity field  $\mathbf{v}$ ; instead, it directly predicts the clean sample  $\hat{\mathbf{x}}$  (as shown in Figure 1):

$$\hat{\mathbf{x}} = f_{\theta}(\mathbf{z}_t, t, \mathbf{cond}), \tag{7}$$

where  $\mathbf{cond}$  denotes the additional conditioning information. In our implicit structural modeling task,  $\mathbf{cond}$  specifically represents the input horizons and faults. Consequently, the predicted velocity field  $\hat{\mathbf{v}}$  can be obtained from  $\hat{\mathbf{x}}$  by differentiating the interpolation path in Eq. 1:

$$\hat{\mathbf{v}} = \hat{\mathbf{x}} - \frac{\mathbf{z}_t - t\hat{\mathbf{x}}}{1-t} = \frac{\hat{\mathbf{x}} - \mathbf{z}_t}{1-t} \tag{8}$$

Based on Eq. 2, we can still compute the  $v$ -loss in Eq. 4 for this velocity estimate. This is the  $\mathbf{x}$ -prediction diffusion formulation adopted in this work. We next introduce the denoising network used in this diffusion framework, which further strengthens structural guidance through explicit conditioning.

## 2.2 Structure-Enhanced Denoising Transformer

We adopt a standard Vision Transformer (ViT) backbone as the denoising network  $f_{\theta}$  (Peebles and Xie, 2023). Since predicting a clean sample on a low-dimensional data manifold is generally easier than regressing the velocity field (Karras et al., 2022), larger patch sizes can be used without sacrificing training stability. In this work, we employ ViT-Base/32 as the backbone, which provides a good trade-off between generation quality and efficiency.

Let  $P = 32$  be the patch size and  $N = (\frac{H}{P}) \times (\frac{W}{P})$  the number of patches. We tokenize  $\mathbf{z}_t$  into a sequence of patch tokens using a bottleneck patch embedding (Alemi et al., 2016), which helps stabilize training:

$$\mathbf{z}_{\mathbf{x}} = \phi_{\mathbf{x}}(\mathbf{z}_t) \in \mathbb{R}^{N \times d}, \quad \phi_{\mathbf{x}}(\cdot) = \text{Conv}_{1 \times 1}(\text{Conv}_{P \times P}(\cdot)), \tag{9}$$

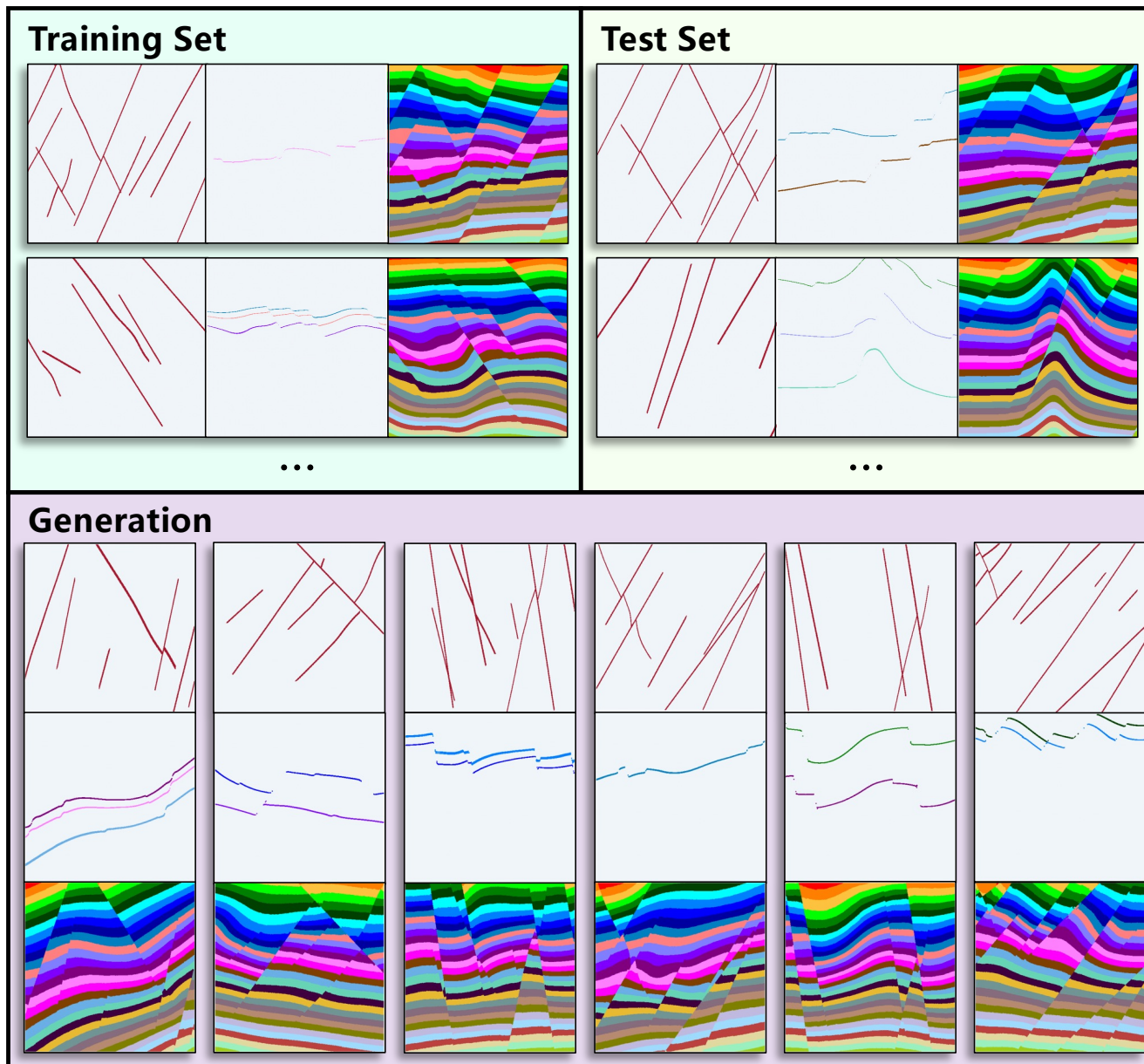


**Figure 2.** Synthetic dataset examples used for training, testing, and conditional generation. Top: representative samples from the training set (left) and test set (right). Bottom: conditional generations from LFD.

where  $\text{Conv}_{P \times P}$  denotes a 2D convolution with kernel size  $P \times P$  and stride  $P$  (thus extracting non-overlapping patch features), and  $\text{Conv}_{1 \times 1}$  denotes a  $1 \times 1$  convolution that linearly projects the bottleneck features to the ViT hidden dimension



We encode horizons and faults using two separate bottleneck embedding modules. Denote the horizon input by  $\mathbf{h}$  and the fault input by  $\mathbf{f}$ . Their token embeddings are

$$\mathbf{z}_h = \phi_h(\mathbf{h}), \quad \mathbf{z}_f = \phi_f(\mathbf{f}), \quad (10)$$

where  $\phi_h(\cdot)$  and  $\phi_f(\cdot)$  have the same bottleneck architecture as  $\phi_x(\cdot)$  but are parameterized independently. For positional encoding of ViTs, we use sine–cosine embeddings to provide a stable global reference and rotary position embedding (RoPE) (Su et al., 2024) to improve relative position modeling, which improves generalization to varying input sizes (Heo et al., 2024).

We fuse the noisy tokens with structural tokens by element-wise addition, a common token-fusion strategy in Transformers that combines multiple embeddings while keeping the token dimension and sequence length unchanged (Peebles and Xie, 2023):

$$\mathbf{z}^{(0)} = \mathbf{z}_x + \mathbf{z}_h + \mathbf{z}_f, \quad (11)$$

where  $\mathbf{z}^{(0)} \in \mathbb{R}^{N \times d}$  denotes the fused token sequence at the input of the Transformer.

Beyond the input-level fusion, we further strengthen structural guidance by injecting horizon and fault embeddings into each Transformer layer as residual priors. Specifically, given the intermediate tokens  $\mathbf{z}^{(\ell)}$ , we form a structure-enhanced representation by

$$\tilde{\mathbf{z}}^{(\ell)} = \mathbf{z}^{(\ell)} + \alpha_\ell \mathbf{z}_h + \beta_\ell \mathbf{z}_f, \quad (12)$$

where  $\alpha_\ell$  and  $\beta_\ell$  are learnable, layer-adaptive weights that control how strongly each layer uses horizon and fault priors. Finally, we obtain  $\hat{\mathbf{x}}$  using Eq. 7 with  $\mathbf{cond} = (\mathbf{h}, \mathbf{f})$ , where the residual injections encourage structure-consistent denoising across layers.

To further strengthen the role of the input structural constraints in guiding generation, we next introduce prior-guided loss terms designed directly in the data space.

### 2.3 Prior-Guided Losses

As the model directly predicts the clean data  $\hat{\mathbf{x}}$ , geological observations and prior constraints can be imposed in a straightforward and differentiable manner. We introduce two prior-guided terms, a horizon loss  $\mathcal{L}_{\text{Hrz}}$  and a fault-aware bending-energy regularizer  $\mathcal{L}_{\text{Bend}}$ , to enforce consistency with the input horizons while promoting smoothness within stratigraphic blocks without smoothing across faults.

The implicit structural model is required to align with the input horizons. Let  $\mathbf{M}_h \in \{0, 1\}^{H \times W}$  be a binary mask derived from the input horizon data, indicating horizon locations. We penalize deviations on the horizon by the mean absolute error normalized by the summed target magnitude:

$$\mathcal{L}_{\text{Hrz}} = \frac{\|\mathbf{M}_h \odot (\hat{\mathbf{x}} - \mathbf{x})\|_1}{\|\mathbf{M}_h \odot \mathbf{x}\|_1 + c}, \quad (13)$$

where  $\odot$  denotes element-wise multiplication and  $c$  is a small constant. This normalization reduces sensitivity to the absolute scale of implicit structural model values.

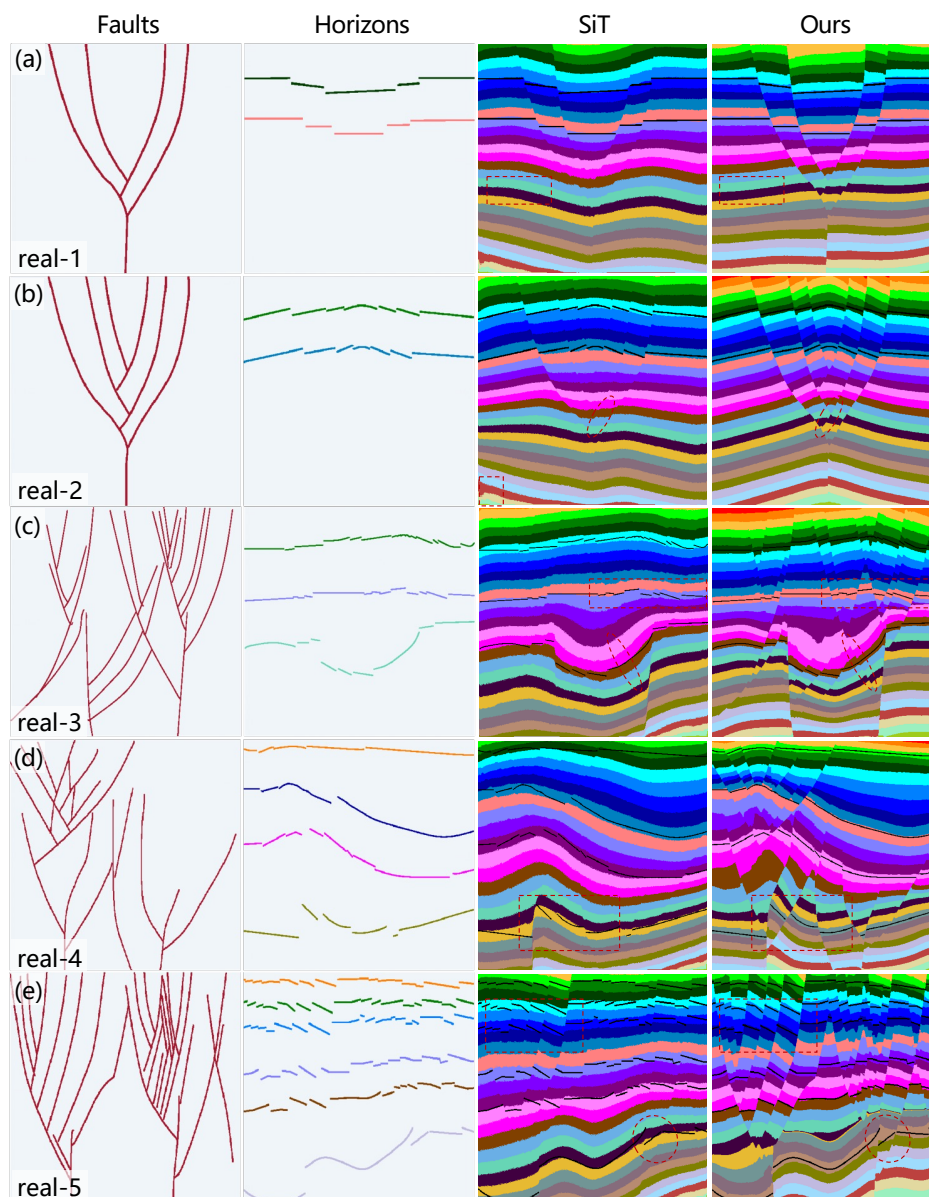


**Figure 3.** Field data results on flower-structure faulting. (a–e) Five real-survey examples with progressively increasing structural complexity from Huang and Liu (2017). From left to right, each row shows the input fault interpretation, the input horizon constraints, the implicit structural model generated by SiT, and the result produced by our method.

Additionally, implicit structural models are expected to form a globally smooth field, and horizons should not exhibit excessive curvature in a geologically reasonable interpretation. We therefore introduce a bending-energy regularizer (Renaudeau et al., 2019; Belhachmi et al., 2025) that penalizes second-order variations of the predicted implicit scalar field. Importantly,



185 this smoothness prior should not be enforced across faults, since faults correspond to discontinuities. To honour fault discontinuities, we compute the bending energy only on the non-fault region and use fault-aware finite-difference stencils that do not cross fault pixels.

Let  $\mathbf{M}_f \in \{0, 1\}^{H \times W}$  denote the input fault mask, and define the fault domain  $\Omega_{\text{Faults}} = \{(i, j) \mid \mathbf{M}_f(i, j) = 1\}$ . The fault-aware bending-energy loss is defined as

$$190 \quad \mathcal{L}_{\text{Bend}} = \mathbb{E}_{(i,j) \notin \Omega_{\text{Faults}}} \left[ \left( \frac{\partial^2 \hat{\mathbf{x}}}{\partial i^2} \right)^2 + 2 \left( \frac{\partial^2 \hat{\mathbf{x}}}{\partial i \partial j} \right)^2 + \left( \frac{\partial^2 \hat{\mathbf{x}}}{\partial j^2} \right)^2 \right], \quad (14)$$

where the second-order derivatives are implemented with fault-aware discrete operators that ignore stencils crossing fault pixels. The final training objective combines the flow matching loss with the prior-guided losses:

$$\mathcal{L} = \mathcal{L}_v + \lambda_{\text{Hrz}} \mathcal{L}_{\text{Hrz}} + \lambda_{\text{Bend}} \mathcal{L}_{\text{Bend}}, \quad (15)$$

where  $\lambda_{\text{Hrz}}$  and  $\lambda_{\text{Bend}}$  are weighting factors used to balance the relative magnitudes of different loss terms during training. In practice, we set  $\lambda_{\text{Hrz}} = 10$  and  $\lambda_{\text{Bend}} = 0.1$  to keep  $\mathcal{L}_v$ ,  $\mathcal{L}_{\text{Hrz}}$ , and  $\mathcal{L}_{\text{Bend}}$  on comparable scales throughout training, thereby avoiding any single term dominating the gradients and ensuring stable optimization.

These design choices define the overall LFD framework, combining  $\mathbf{x}$ -prediction with the  $v$ -loss, structure-enhanced denoising transformers, and data-space prior-guided regularization. In the following, we evaluate its effectiveness on synthetic data and challenging field examples.

## 200 3 Experiments

### 3.1 Data Preparation

To train and validate our conditional generative diffusion model for implicit structural modeling, we construct a large synthetic dataset in two stages: (i) geology-informed 3D structural simulation and (ii) conversion to 2D conditional training pairs (as shown in Figure 2).

205 First, we generate realistic 3D implicit structural models using a simulation workflow in the spirit of Wu et al. (2020). Folding deformation is created by superposing multiple parameterized Gaussian functions, with key parameters randomly sampled to cover a wide range of fold wavelengths, amplitudes, and asymmetries. We then introduce geologically plausible faulting by constructing 3D fault surfaces, assembling fault networks (fault assemblages), and simulating 3D slip distributions between the hanging wall and footwall. Building on the resulting folded–faulted framework, we further incorporate unconformities and associated stratal termination patterns (e.g., onlap, downlap, toplap, and related terminations). This procedure yields 3000 realistic 3D implicit structural models at  $512 \times 512 \times 512$  resolution, each paired with a full-volume 3D fault mask. The combination of explicit fold/fault/unconformity rules and controlled parameter randomization ensures both geological plausibility and broad structural–stratigraphic diversity across the dataset.

215 Second, to match our 2D conditional diffusion training setup, we randomly extract  $512 \times 512$  slices from the 3D volumes of implicit models and fault masks along both inline and crossline directions to increase directional variability and improve

**Table 1.** Model parameter counts.

Parameter	VAE	Diffusion	Total
SiT-B/2	101.14 M	144.55 M	245.69 M
LFD (ViT-B/32)	–	145.42 M	<b>145.42 M</b>

generalization. From each 2D implicit model (used as the target label ( $\mathbf{x}$ )), we derive conditioning inputs in two forms: (1) the corresponding full 2D fault mask ( $\mathbf{f}$ ), providing complete fault-boundary conditions, and (2) sparse and potentially incomplete horizon constraints ( $\mathbf{h}$ ) obtained by randomly sampling a small set of horizons or horizon segments (following Bi et al., 2022) to mimic practical interpretation scenarios. These complementary conditions—global fault geometry from ( $\mathbf{f}$ ) and sparse stratigraphic cues from ( $\mathbf{h}$ )—jointly guide the conditional diffusion model to generate structurally consistent implicit scalar fields. In total, we construct 64,000 training pairs  $\{(\mathbf{h}, \mathbf{f}), \mathbf{x}\}$ , and normalize both inputs and target implicit fields to  $[-1, 1]$  to stabilize training.

For field-data evaluation, we test on several real-survey cases from Huang and Liu (2017), characterized by complex flower-structure faulting with associated horizon interpretations, as shown in the first two columns of Figure 3. We denote the five cases in Figure 3(a–e) as *real-1* through *real-5*, respectively. Since implicit scalar field values on horizons are unavailable in real surveys, we assign normalized horizon values by mapping the mean horizon depth ratio linearly to  $[-1, 1]$ , providing a consistent relative ordering of horizons for conditioning.

### 3.2 Training Settings

We initialize the ViT-Base/32 backbone with pretrained weights from Li and He (2025). We set the noise scale to 0.2 when constructing noisy samples during training because it yields smoother implicit fields in our experiments. We discuss the impact of noise scale in Sect. 4. We use a learning rate of  $5 \times 10^{-5}$  with a batch size of 128 and train for 600 epochs. Training is performed on three 96 GB NVIDIA H20 GPUs and takes approximately 18 h. At inference, we discretize the ODE integration into  $K = 50$  steps for all experiments.

For comparison, we implement a latent-diffusion baseline that follows the SiT (Ma et al., 2024) training paradigm with a pretrained VAE (Rombach et al., 2022). As reported in Table 1, our model (LFD) and the SiT baseline have comparable parameter counts, making the comparison fair. All models are trained under the same settings as above.

### 3.3 Evaluation Metric

To quantify horizon adherence on real surveys, where ground-truth implicit structural models are unavailable, we propose the *Horizon Consistency Error* (HCE), which measures how consistent the predicted implicit field values are along each input horizon. Let  $\hat{\mathbf{x}} \in \mathbb{R}^{H \times W}$  denote the generated implicit model, and let  $\mathbf{H} \in \{0, 1, \dots\}^{H \times W}$  be the horizon label map, where  $\mathbf{H}(i, j) = 0$  indicates background and  $\mathbf{H}(i, j) = k$  denotes the  $k$ -th horizon. For each horizon  $k \in \mathcal{K} = \{k | k \neq 0\}$ , we define



**Table 2.** Inference times.

Time (s)	VAE Enc	Diffusion	VAE Dec	Total
SiT-B/2	0.95	1.60	0.07	2.63
LFD (ViT-B/32)	–	<b>1.56</b>	–	<b>1.56</b>

**Table 3.** Values of Horizon Consistency Error (HCE) on field data shown in Figure 3.

HCE (1e-3) ↓	real-1	real-2	real-3	real-4	real-5
SiT-B/2	6.17	6.62	13.41	16.33	16.42
LFD (ViT-B/32)	<b>3.05</b>	<b>3.59</b>	<b>3.64</b>	<b>2.97</b>	<b>6.17</b>

the horizon support

$$\Omega_k = \{(i, j) \mid \mathbf{H}(i, j) = k\}. \tag{16}$$

We first compute the mean implicit value on that horizon,

$$245 \quad \mu_k = \frac{1}{|\Omega_k|} \sum_{(i,j) \in \Omega_k} \hat{\mathbf{x}}(i, j), \tag{17}$$

and then measure the mean absolute deviation from this mean:

$$e_k = \frac{1}{|\Omega_k|} \sum_{(i,j) \in \Omega_k} |\hat{\mathbf{x}}(i, j) - \mu_k|. \tag{18}$$

If the generated implicit field is well aligned with the  $k$ -th horizon,  $\hat{\mathbf{x}}$  should be nearly constant along  $\Omega_k$ , yielding  $e_k \approx 0$ ; otherwise,  $e_k$  increases as  $\hat{\mathbf{x}}$  varies along the horizon. Finally, we aggregate the per-horizon errors using a pixel-wise normalized

250 average:

$$\mathcal{M}_{\text{HCE}} = \frac{\sum_k |\Omega_k| e_k}{\sum_k |\Omega_k|}. \tag{19}$$

This pixel-wise normalized aggregation avoids dependence on the number and length of horizons, enabling fair comparisons across cases.

### 3.4 Results

255 Figure 2 shows representative synthetic test examples. The generated implicit models honor the input faults and horizons and produce sharp, fault-aligned discontinuities. This indicates that the structural constraints are effectively enforced during generation. Benefiting from large-patch inference, generating a  $512 \times 512$  implicit model requires only 1.56 s on a single NVIDIA H20 GPU. This runtime is measured with batch size 1 by generating 20 samples and reporting the average per-sample time. As summarized in Table 2, our method is faster than the SiT baseline, largely because the larger patch size

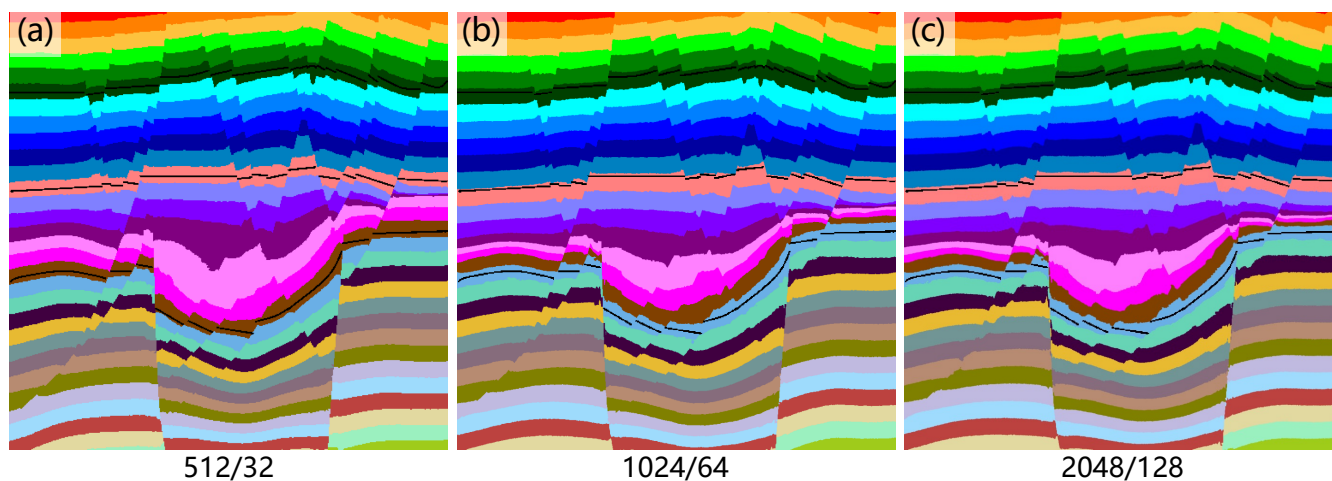


**Figure 4.** Resolution generalization. The model trained at  $512 \times 512$  is directly applied to higher resolutions by adjusting the patch size to keep the token grid fixed. From left to right: 512/32, 1024/64, and 2048/128 (resolution/patch size). The model preserves high-quality implicit structural predictions at  $1024 \times 1024$  and  $2048 \times 2048$  without additional training.

260 reduces token length and attention cost. Moreover, SiT additionally incurs VAE encoding and decoding overhead, further widening the efficiency gap.

We further evaluate the method on five challenging real-survey cases with complex flower-structure faulting (Figure 3). As shown in Figure 3(a–e), the structural complexity increases progressively from *real-1* to *real-5*, placing higher demands on both fault continuity and horizon conformity. The SiT baseline (third column in Figure 3) can recover the major faults, 265 but without explicit geological priors its generated implicit models tend to drift away from the input horizons, which in turn degrades finer-scale stratigraphic features.

Beyond this overall trend, the visual comparisons in Figure 3 highlight several characteristic behaviors. In panel (a), the red box shows that SiT exhibits noticeably stronger noise than our method, which may be related to the sensitivity of VAE decoding to latent perturbations that can be amplified into artifacts in the implicit field (Liu et al., 2026). In panel (b), the red box 270 reveals anomalous values in the SiT result, indicating potential instabilities in latent-space generation. Moreover, the red ellipse indicates that our method can still enforce a fault-aligned discontinuity in the implicit field even where horizon constraints are sparse, whereas SiT fails to express the fault geometry at that location. In panels (d) and (e), the red boxes further demonstrate that our method remains better anchored to the input horizons and produces sharper, more clearly delineated fault boundaries. We also note a challenging region in panel (e) (red ellipse), where both methods deviate from the input horizons due to the 275 presence of pronounced thrusting, making faithful recovery particularly difficult. This represents a limitation of our current approach; nevertheless, our method still achieves relatively improved horizon conformity compared with SiT in this setting.

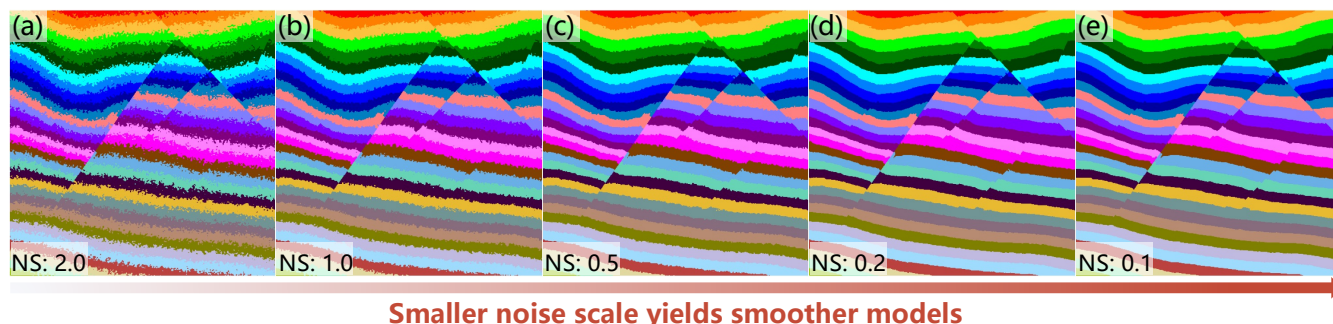


**Figure 5.** Effect of noise scale (NS) on generation. The model is trained with noise scale  $NS = 2.0$ . During inference, we vary only the noise scale while keeping all other settings fixed. Panels (a–e) correspond to  $NS = \{2.0, 1.0, 0.5, 0.2, 0.1\}$ . As NS decreases, the generated implicit structural models become smoother and exhibit less residual noise.

The above visual comparisons are quantitatively confirmed by the error metrics given in Table 3, which show that our approach achieves better horizon consistency than SiT, consistent with Figure 3 and highlighting the value of explicitly injecting geological priors for reliable implicit structural modeling in complex real surveys.

## 280 4 Discussion

In developing LFD, we observed several interesting behaviors that provide additional insight into diffusion-based implicit structural modeling, while also revealing practical limitations of the current study. We summarize these findings below.

**Resolution robustness.** Our model is trained on  $512 \times 512$  samples, yet we observe encouraging robustness to higher resolutions. In principle, the same adaptation applies to other larger input sizes; here we use  $1024 \times 1024$  and  $2048 \times 2048$  as  
 285 representative examples. In testing, we upsample the input horizons and faults to  $1024 \times 1024$  and  $2048 \times 2048$  using nearest-neighbor interpolation. To keep the token length unchanged (i.e., a  $16 \times 16$  token grid), we increase the patch size to  $P = 64$  and  $P = 128$  for 1024 and 2048 inputs, respectively. For each bottleneck patch embedding module, the spatial grid changes with resolution; therefore, we interpolate the positional embeddings and reuse the pretrained network parameters accordingly to adapt the model to the new grid. Surprisingly, the generated implicit models remain high-quality at both 1024 and 2048  
 290 resolutions (Figure 4). We attribute this behavior partly to the relative positional encoding (RoPE), which provides a degree of resolution robustness by expressing positions in a scale-consistent manner. This observation is consistent with prior findings that RoPE improves resolution extrapolation in vision transformers (Heo et al., 2024; van de Geijn et al., 2025). We note, however, that this finding may be task-dependent: implicit structural models are typically smooth fields and do not require extremely high-frequency details.

**Impact of noise scale.** We find that the noise scale is a critical factor for implicit structural modeling. In early experiments,  
 295 using commonly adopted noise scales for natural-image diffusion (e.g., 1.0 or 2.0) often led to overly noisy generations even with prolonged training. This is likely because implicit structural models exhibit relatively smooth distributions, for which



excessively strong corruption can hinder stable denoising. We perform an ablation study on the noise scale (Figure 5) and observe that decreasing the noise scale yields noticeably smoother and more geologically reasonable implicit fields. This finding provides practical guidance for deploying diffusion models on high-dimensional geophysical data: the noise scale should be tuned to the target task and data characteristics to achieve optimal generation quality.

**Conditioning flexibility and applicability.** We only consider faults and horizons as conditioning inputs in this work. For practical implicit structural modeling, additional information such as interpreted normals or orientation constraints are often beneficial, and we believe they can be incorporated naturally in our framework, either as extra input channels or as explicit loss terms. Compared with VAE-based latent diffusion, injecting such geological priors in our data-space approach is more direct and interpretable, avoiding the ambiguity of enforcing constraints in a learned latent space. Moreover, our formulation enables flexible generation of implicit structural model samples. With only a few sketched horizons and faults, the model can produce geologically realistic implicit fields, which facilitates the construction and iterative refinement of structural modeling datasets compared with traditional workflows that often rely on computationally intensive physics-based forward modeling.

**Limitation and 3D extension.** This study primarily focuses on validating the effectiveness of  $x$ -prediction, the structure-enhanced transformer design, and the proposed prior-guided losses. Accordingly, our experiments are conducted on 2D implicit structural modeling, which does not fully capture 3D geological complexity such as fault connectivity and branching. Nevertheless, the proposed framework is conceptually extendable to 3D by replacing 2D patch embeddings and attention with their 3D counterparts. However, a practical 3D implementation requires additional considerations due to the substantially increased computational cost and the higher structural complexity of volumetric faulted settings. Future work will evaluate the full 3D extension, including computational scaling and constraint satisfaction in volumetric settings.

## 5 Conclusions

To eliminate reliance on VAE-based latent compression in high-dimensional diffusion modeling and overcome the difficulty of imposing geological priors in latent space, we propose LFD, a latent-compression-free, prior-guided diffusion framework with denoised-sample prediction for implicit structural modeling. LFD uses flow matching but predicts the implicit structural model directly in data space. This keeps the modeling target explicit and makes it easier to enforce geological constraints. We design a structure-enhanced ViT to improve conditioning. The network injects horizon and fault information at multiple layers. We also add two prior-guided losses. The horizon loss enforces consistency on horizon locations. The fault-aware bending-energy loss penalizes curvature only within fault-bounded regions. It avoids stencils across faults and preserves sharp discontinuities. Experiments on synthetic data and five real-survey examples with complex flower-structure faulting show that LFD produces more coherent implicit structural models than SiT. Generally, LFD provides new insights for combining diffusion modeling with prior-guided constraints on high-dimensional geophysical data.



## 6 Code and data availability

The source code of this study is openly available on Zenodo at <https://doi.org/10.5281/zenodo.18772173> (Guo et al., 2026).

## 330 7 Author contribution

Z.G. carried out the experiments, performed the analysis, and drafted the manuscript. X.W. proposed the main ideas, supervised the work, and revised the manuscript. Y.D. collected and curated the data. H.G. contributed to the discussion and revised the manuscript. G.C. contributed to the discussion and revised the manuscript.

## 8 Competing interests

335 The authors declare that they have no conflict of interest.

*Acknowledgements.* This study was financially supported by the DeepEarth Probe and Mineral Resources Exploration-National Science and Technology Major Project under the grant 2024ZD1002100. Z.G. acknowledges support from the China Scholarship Council under the Joint Ph.D. Program for his mobility scholarship at Université de Lorraine. G.C. acknowledges the sponsors of the RING Consortium ([ring-team.org/consortium](http://ring-team.org/consortium)).



## 340 References

- Alemi, A. A., Fischer, I., Dillon, J. V., and Murphy, K.: Deep variational information bottleneck, arXiv preprint arXiv:1612.00410, 2016.
- Arienti, G., Bistacchi, A., Caumon, G., Monopoli, B., and Dal Piaz, G.: 3D structural implicit modelling of folded metamorphic units at Lago di Cignana with uncertainty assessment, *Journal of Structural Geology*, 191, 105–114, 2025.
- Belhachmi, A., Benabbou, A., and Mourrain, B.: A spline-based regularized method for the reconstruction of complex geological models,  
345 *Mathematical Geosciences*, 57, 89–114, 2025.
- Bi, Z., Wu, X., Geng, Z., and Li, H.: Deep relative geologic time: A deep learning method for simultaneously interpreting 3-D seismic horizons and faults, *Journal of Geophysical Research: Solid Earth*, 126, e2021JB021 882, 2021.
- Bi, Z., Wu, X., Li, Z., Chang, D., and Yong, X.: DeepISMNet: Three-dimensional implicit structural modeling with convolutional neural network, *Geoscientific Model Development Discussions*, 2022, 1–28, 2022.
- 350 Bonnaire, T., Urfin, R., Biroli, G., and Mézard, M.: Why Diffusion Models Don't Memorize: The Role of Implicit Dynamical Regularization in Training, arXiv preprint arXiv:2505.17638, 2025.
- Calcagno, P., Chilès, J.-P., Courrioux, G., and Guillen, A.: Geological modelling from field data and geological knowledge: Part I. Modelling method coupling 3D potential-field interpolation and geological rules, *Physics of the Earth and Planetary Interiors*, 171, 147–157, 2008.
- Caumon, G., Collon-Drouaillet, P., Le Carlier de Veslud, C., Viseur, S., and Sausse, J.: Surface-based 3D modeling of geological structures,  
355 *Mathematical geosciences*, 41, 927–945, 2009.
- Caumon, G., Gray, G., Antoine, C., and Titeux, M.-O.: Three-dimensional implicit stratigraphic model building from remote sensing data on tetrahedral meshes: theory and application to a regional model of La Popa Basin, NE Mexico, *IEEE Transactions on Geoscience and Remote Sensing*, 51, 1613–1621, 2013.
- Chapelle, O., Scholkopf, B., and Zien, A.: Semi-supervised learning (chapelle, o. et al., eds.; 2006)[book reviews], *IEEE Transactions on*  
360 *Neural Networks*, 20, 542–542, 2009.
- Chilès, J.-P., Aug, C., Guillen, A., and Lees, T.: Modelling the geometry of geological units and its uncertainty in 3D from structural data: the potential-field method, in: *Proceedings of international symposium on orebody modelling and strategic mine planning*, Perth, Australia, vol. 22, p. 24, 2004.
- Choi, J., Kim, S., Jeong, Y., Gwon, Y., and Yoon, S.: Ilvr: Conditioning method for denoising diffusion probabilistic models, arXiv preprint  
365 arXiv:2108.02938, 2021.
- Cowan, E., Beatson, R., Fright, W., McLennan, T., and Mitchell, T.: Rapid geological modelling, in: *Applied structural geology for mineral exploration and mining*, international symposium, pp. 23–25, 2002.
- Dao, Q., Phung, H., Nguyen, B., and Tran, A.: Flow matching in latent space, arXiv preprint arXiv:2307.08698, 2023.
- De la Varga, M., Schaaf, A., and Wellmann, F.: GemPy 1.0: open-source stochastic geological modeling and inversion, *Geoscientific Model*  
370 *Development*, 12, 1–32, 2019.
- Fan, W., Azevedo, L., Liu, G., Chen, Q., Wu, X., and Li, Y.: Automatic reconstruction of 3D geological models based on Recurrent Neural Network and predictive learning, *Computers & Geosciences*, p. 105996, 2025.
- Frank, T.: *Advanced visualization and modeling of tetrahedral meshes*, Gesellschaft für Informatik, 2007.
- Gao, K. and Wellmann, F.: Fault representation in structural modelling with implicit neural representations, *Computers & Geosciences*, 199,  
375 105 911, 2025.



- Garayt, C., Desassis, N., Blusseau, S., Gibert, P.-M., Langanay, J., and Romary, T.: Two-dimensional stochastic structural geomodeling with deep generative adversarial networks, *Mathematical Geosciences*, 57, 1095–1114, 2025.
- Gat, I., Remez, T., Shaul, N., Kreuk, F., Chen, R. T., Synnaeve, G., Adi, Y., and Lipman, Y.: Discrete flow matching, *Advances in Neural Information Processing Systems*, 37, 133 345–133 385, 2024.
- 380 Gillberg, T., Bruaset, A. M., Hjelle, Ø., and Sourouri, M.: Parallel solutions of static Hamilton-Jacobi equations for simulations of geological folds, *Journal of Mathematics in Industry*, 4, 10, 2014.
- Giraud, J., Lindsay, M., Jessell, M., and Ogarko, V.: Towards plausible lithological classification from geophysical inversion: honouring geological principles in subsurface imaging, *Solid Earth*, 11, 419–436, 2020.
- Giraud, J., Caumon, G., Grose, L., Ogarko, V., and Cupillard, P.: Integration of automatic implicit geological modelling in deterministic  
385 geophysical inversion, *Solid Earth*, 15, 63–89, 2024.
- Grose, L., Ailleres, L., Laurent, G., and Jessell, M.: LoopStructural 1.0: time-aware geological modelling, *Geoscientific Model Development*, 14, 3915–3937, 2021.
- Guo, J., Wu, L., Zhou, W., Li, C., and Li, F.: Section-constrained local geological interface dynamic updating method based on the HRBF surface, *Journal of Structural Geology*, 107, 64–72, 2018.
- 390 Guo, Z., Wu, X., Liang, L., Sheng, H., Chen, N., and Bi, Z.: Cross-domain foundation model adaptation: Pioneering computer vision models for geophysical data analysis, *Journal of Geophysical Research: Machine Learning and Computation*, 2, e2025JH000 601, 2025.
- Guo, Z., Wu, X., Dou, Y., Gao, H., and Caumon, G.: Code from “Latent-Compression-Free Generative Diffusion with Geological Priors and Geophysical Regularization for Implicit Structural Modeling”, <https://doi.org/10.5281/zenodo.18772173>, 2026.
- Heo, B., Park, S., Han, D., and Yun, S.: Rotary position embedding for vision transformer, in: *European Conference on Computer Vision*,  
395 pp. 289–305, Springer, 2024.
- Hillier, M., Wellmann, F., Brodaric, B., de Kemp, E., and Schetselaar, E.: Three-dimensional structural geological modeling using graph neural networks, *Mathematical geosciences*, 53, 1725–1749, 2021.
- Hillier, M., Wellmann, F., de Kemp, E. A., Brodaric, B., Schetselaar, E., and Bedard, K.: GeoINR 1.0: an implicit neural network approach to three-dimensional geological modelling, *Geoscientific Model Development*, 16, 6987–7012, 2023.
- 400 Hjelle, Ø. and Petersen, S. A.: A Hamilton–Jacobi framework for modeling folds in structural geology, *Mathematical Geosciences*, 43, 741–761, 2011.
- Ho, J., Jain, A., and Abbeel, P.: Denoising diffusion probabilistic models, *Advances in neural information processing systems*, 33, 6840–6851, 2020.
- Houlding, S.: *3D Geoscience Modeling: Computer Techniques for Geological Characterization*, *3D Geoscience Modeling: Computer  
405 Techniques for Geological Characterization*, Springer-Verlag, ISBN 9783540580157, <https://books.google.fr/books?id=a04SAQAIAAJ>, 1994.
- Huang, L. and Liu, C.-y.: Three types of flower structures in a divergent-wrench fault zone, *Journal of Geophysical Research: Solid Earth*, 122, 10–478, 2017.
- Irakarama, M., Thierry-Coudon, M., Zakari, M., and Caumon, G.: Finite element implicit 3D subsurface structural modeling, *Computer-  
410 Aided Design*, 149, 103 267, 2022.
- Kamath, A. V., Thiele, S. T., Moulard, M., Grose, L., Tolosana-Delgado, R., Hillier, M., Wellmann, F., and Gloaguen, R.: Curlew 1.0: Spatio-temporal implicit geological modelling with neural fields in python, 2025.



- Karras, T., Aittala, M., Aila, T., and Laine, S.: Elucidating the design space of diffusion-based generative models, *Advances in neural information processing systems*, 35, 26 565–26 577, 2022.
- 415 Lajaunie, C., Courrioux, G., and Manuel, L.: Foliation fields and 3D cartography in geology: principles of a method based on potential interpolation, *Mathematical geology*, 29, 571–584, 1997.
- Lee, D., Ovanger, O., Eidsvik, J., Aune, E., Skauvold, J., and Hauge, R.: Latent diffusion model for conditional reservoir facies generation, *Computers & Geosciences*, 194, 105 750, 2025.
- Li, T. and He, K.: Back to basics: Let denoising generative models denoise, *arXiv preprint arXiv:2511.13720*, 2025.
- 420 Li, X., Zhao, J., and Zhou, S.: Implicit neural representations for 3D gravity inversion, *Computers & Geosciences*, p. 106082, 2025.
- Lin, L., Li, C., Wei, H., Zhong, Z., Wang, X., Li, Q., and Gorman, A.: An improved parametric 3D geologic modeling framework for seismic structure identification using deep learning in complex geologic settings, *Geophysics*, 90, IM81–IM102, 2025.
- Lipman, Y., Chen, R. T., Ben-Hamu, H., Nickel, M., and Le, M.: Flow matching for generative modeling, *arXiv preprint arXiv:2210.02747*, 2022.
- 425 Liu, S., Qin, C., Yin, H., Yan, Q., Duan, Z.-P., Li, C., Lyu, J., Guo, C.-L., and Li, C.: Improving Reconstruction of Representation Autoencoder, *arXiv preprint arXiv:2602.08620*, 2026.
- Liu, X., Gong, C., and Liu, Q.: Flow straight and fast: Learning to generate and transfer data with rectified flow, *arXiv preprint arXiv:2209.03003*, 2022.
- Liu, Y. and Durlofsky, L. J.: 3D CNN-PCA: A deep-learning-based parameterization for complex geomodels, *Computers & Geosciences*,  
430 148, 104 676, 2021.
- Ma, N., Goldstein, M., Albergo, M. S., Boffi, N. M., Vanden-Eijnden, E., and Xie, S.: Sit: Exploring flow and diffusion-based generative models with scalable interpolant transformers, in: *European Conference on Computer Vision*, pp. 23–40, Springer, 2024.
- MacCormack, K. E., Rokosh, D., and Branscombe, P.: Chapter 5: The Alberta Geological Survey 3D Geological Modelling Program, <https://api.semanticscholar.org/CorpusID:208368942>, 2019.
- 435 Mallet, J.-L.: Discrete smooth interpolation, *ACM Transactions on Graphics (TOG)*, 8, 121–144, 1989.
- Mallet, J.-L.: Space–time mathematical framework for sedimentary geology, *Mathematical geology*, 36, 1–32, 2004.
- Mallet, J.-L.: *Elements of mathematical sedimentary geology: The GeoChron model*, EAGE, 2014.
- Maxelon, M., Renard, P., Courrioux, G., Brändli, M., and Mancktelow, N.: A workflow to facilitate three-dimensional geometrical modelling of complex poly-deformed geological units, *Computers & Geosciences*, 35, 644–658, 2009.
- 440 Nichol, A. Q. and Dhariwal, P.: Improved denoising diffusion probabilistic models, in: *International conference on machine learning*, pp. 8162–8171, PMLR, 2021.
- Osher, S.: A level set formulation for the solution of the Dirichlet problem for Hamilton–Jacobi equations, *SIAM Journal on Mathematical Analysis*, 24, 1145–1152, 1993.
- Peebles, W. and Xie, S.: Scalable diffusion models with transformers, in: *Proceedings of the IEEE/CVF international conference on computer vision*, pp. 4195–4205, 2023.
- 445 Pizzella, L., Alais, R., Lopez, S., Freulon, X., and Rivoirard, J.: Taking better advantage of fold axis data to characterize anisotropy of complex folded structures in the implicit modeling framework, *Mathematical Geosciences*, 54, 95–130, 2022.
- Ren, A., Wu, L., Xu, J., Xing, Y., Qiu, Q., and Xie, Z.: A deep learning method for 3D geological modeling using ET4DD with offset-attention mechanism, *Computers & Geosciences*, 200, 105 929, 2025.



- 450 Renaudeau, J., Malvesin, E., Maerten, F., and Caumon, G.: Implicit structural modeling by minimization of the bending energy with moving least squares functions, *Mathematical Geosciences*, 51, 693–724, 2019.
- Rombach, R., Blattmann, A., Lorenz, D., Esser, P., and Ommer, B.: High-resolution image synthesis with latent diffusion models, in: *Proceedings of the IEEE/CVF conference on computer vision and pattern recognition*, pp. 10 684–10 695, 2022.
- Shah, K., Kalavasis, A., Klivans, A. R., and Daras, G.: Does generation require memorization? creative diffusion models using ambient  
455 diffusion, arXiv preprint arXiv:2502.21278, 2025.
- Sheng, H., Wu, X., Si, X., Li, J., Zhang, S., and Duan, X.: Seismic foundation model: A next generation deep-learning model in geophysics, *Geophysics*, 90, IM59–IM79, 2025.
- Sohl-Dickstein, J., Weiss, E., Maheswaranathan, N., and Ganguli, S.: Deep unsupervised learning using nonequilibrium thermodynamics, in: *International conference on machine learning*, pp. 2256–2265, pmlr, 2015.
- 460 Song, B., Kwon, S. M., Zhang, Z., Hu, X., Qu, Q., and Shen, L.: Solving inverse problems with latent diffusion models via hard data consistency, arXiv preprint arXiv:2307.08123, 2023.
- Su, J., Ahmed, M., Lu, Y., Pan, S., Bo, W., and Liu, Y.: Roformer: Enhanced transformer with rotary position embedding, *Neurocomputing*, 568, 127 063, 2024.
- van de Geijn, C., Lüddecke, T., Turishcheva, P., and Ecker, A. S.: A Circular Argument: Does RoPE need to be Equivariant for Vision?, arXiv  
465 preprint arXiv:2511.08368, 2025.
- Vollgger, S. A., Cruden, A. R., Ailleres, L., and Cowan, E. J.: Regional dome evolution and its control on ore-grade distribution: Insights from 3D implicit modelling of the Navachab gold deposit, Namibia, *Ore Geology Reviews*, 69, 268–284, 2015.
- Wang, S., Cai, Z., Si, X., and Cui, Y.: A three-dimensional geological structure modeling framework and its application in machine learning, *Mathematical Geosciences*, 55, 163–200, 2023.
- 470 Wellmann, F. and Caumon, G.: 3-D Structural geological models: Concepts, methods, and uncertainties, in: *Advances in geophysics*, vol. 59, pp. 1–121, Elsevier, 2018.
- Wu, X. and Hale, D.: 3D seismic image processing for unconformities, *Geophysics*, 80, IM35–IM44, 2015.
- Wu, X., Geng, Z., Shi, Y., Pham, N., Fomel, S., and Caumon, G.: Building realistic structure models to train convolutional neural networks for seismic structural interpretation, *Geophysics*, 85, WA27–WA39, 2020.
- 475 Wu, X., Ma, J., Si, X., Bi, Z., Yang, J., Gao, H., Xie, D., Guo, Z., and Zhang, J.: Sensing prior constraints in deep neural networks for solving exploration geophysical problems, *Proceedings of the National Academy of Sciences*, 120, e2219573 120, 2023.
- Yang, L., Hyde, D., Grujic, O., Scheidt, C., and Caers, J.: Assessing and visualizing uncertainty of 3D geological surfaces using level sets with stochastic motion, *Computers & geosciences*, 122, 54–67, 2019.
- Zhang, B., Xu, Z., Wei, X., Song, L., Shah, S. Y. A., Khan, U., Du, L., and Li, X.: Deep subsurface pseudo-lithostratigraphic modeling based  
480 on three-dimensional convolutional neural network (3D CNN) using inversed geophysical properties and shallow subsurface geological model, *Lithosphere*, 2024, lithosphere\_2023\_273, 2024.
- Zheglava, P., Lelièvre, P. G., and Farquharson, C. G.: Multiple level-set joint inversion of traveltimes and gravity data with application to ore delineation: A synthetic study, *Geophysics*, 83, R13–R30, 2018.
- Zhong, D.-y., Lin, B., et al.: Implicit modeling of complex orebody with constraints of geological rules, *Transactions of Nonferrous Metals Society of China*, 29, 2392–2399, 2019.
- 485 Zhou, Z., Chen, D., Wang, C., Chen, C., and Lyu, S.: Simple and fast distillation of diffusion models, *Advances in Neural Information Processing Systems*, 37, 40 831–40 860, 2024.